Received 6 May 2022; accepted 27 May 2022. Date of publication 8 June 2022; date of current version 17 June 2022.

Digital Object Identifier 10.1109/OJAP.2022.3181345

Detection of Failures in Antenna Arrays Through a Lebesgue-Space Approach

VALENTINA SCHENONE[1], ALESSANDRO FEDELI[1] (Member, IEEE), CLAUDIO ESTATICO[2], MATTEO PASTORINO[1] (Fellow, IEEE), AND ANDREA RANDAZZO[1] (Senior Member, IEEE)

[1]Department of Electrical, Electronic, Telecommunications Engineering and Naval Architecture, University of Genoa, 16145 Genoa, Italy

[2]Department of Mathematics, University of Genoa, 16146 Genoa, Italy

CORRESPONDING AUTHOR: A. FEDELI (e-mail: alessandro.fedeli@unige.it)

This work was supported in part by the Italian Ministry for Education, University, and Research through the Project PRIN2017 DI-CA under Grant 20177C3WRM.

ABSTRACT In this paper, a novel antenna array diagnostic approach is presented. The failures in antenna arrays are detected by means of a non-Hilbertian Lebesgue-space L^p technique to solve the underlying inverse problem. The solution of this inverse problem enables to retrieve the distribution of faulty feed excitations of the antenna under test starting from far-field measurements. The developed approach has been numerically validated. Simulations concern planar arrays where different rates and distributions of failures have been tested. Results show good capabilities in detecting damaged regions in the analyzed scenarios.

INDEX TERMS Antenna diagnostics, antenna arrays, inverse source, Lebesgue spaces.

I. INTRODUCTION

NOWADAYS, arrays of antennas are key components in a large number of applications [1]–[4], such as radar, telecommunications, and electromagnetic imaging [5]–[8]. Indeed, by using proper architectures combined with smart synthesis techniques, such antennas may provide enhanced radiation properties and allow reconfiguring the radiation pattern electronically [9], [10].

In this framework, a crucial job consists in array diagnostics. Modern arrays are usually constituted by a large number of elements, and the possibility of detecting and localizing the failures is fundamental for assessing the correct functionalities of the antenna and to recover it in case of damages. Indeed, failures in the array may cause significant deviations in the radiated fields, e.g., variation in the direction of array beam and increment of the sidelobe level. If a proper diagnostic technique to identify the faulty elements is available, only such faulty components can be repaired, to restore the desired radiation characteristics.

In the past years, a wide number of techniques have been proposed to face the problem of antenna diagnostics. Many of them formulate antenna diagnostics as an inverse-source problem [11], [12], with the aim of retrieving the distribution of current over the antenna under test by means of measurements of the radiated field. This inverse problem is usually quite challenging to solve due to the ill-posedness of the related equations. Consequently, ad-hoc algorithms are necessary to tackle this problem [12].

In the scientific literature, at first, the backpropagation procedure (BP) exploiting the Fourier relationship between the field on the array aperture and the far-field measurements has been applied followed by the matrix method (MM) [13]–[15]. Moreover, approaches based on neural networks and machine learning concepts have been developed [16]–[18]. In the last years, several techniques based on the equivalent source reconstruction method (SRM) have also been proposed in this context. These methods allow the reconstruction of an equivalent currents distribution on a surface surrounding the antenna under test (AUT) from near-field measurements through Huygens' principle [19]–[23]. This family of diagnostic procedures has been found effective in using arbitrary-geometry measurements and antenna arrays.

Recently, several methods based on compressive sensing (CS), which is a sparse recovery technique proposed in many research fields including electromagnetic imaging [24]–[29], have also been proposed [30]–[33].

Indeed, in several cases, faulty elements may be represented as a sparse distribution. Moreover, these methods have usually the benefit of requiring a smaller number of measurements (thanks to the a-priori information about sparseness), which results in a lower measurement time.

In this paper, a novel diagnostic technique, based on the use of an inversion scheme performing a regularization in the framework of the Lebesgue spaces L^p, is proposed. In particular, this procedure is applied to solve, in a regularized way, the underlying inverse problem and retrieve the distribution of faulty excitations from measurements of the radiated field performed in the far-field region. It is worth noting that inversion techniques in Lebesgue spaces are potentially able to provide significant enhancements in the reconstruction of the unknowns with respect to both classical Hilbert space approaches and compressive sensing methods. Indeed, both these two kinds of approaches have some limitations. In particular, regularization techniques developed in the framework of Hilbert spaces are usually affected by oversmoothing effects, that may limit the reconstruction of small and sparse solutions. Conversely, compressive sensing techniques, at least in their common formulation, allow obtaining good reconstructions of sparse targets, but may fail when non-sparse unknowns need to be found. Moreover, usually, compressive sensing techniques strictly require that some specific conditions, such as the restricted isometry property (RIP) [29], [34], [35], are satisfied. Instead, Lebesgue-space inversion allows good reconstructions in both conditions. Indeed, it has been found in microwave imaging applications that the use of low values of p allows to promote the sparsity of the solution [36]–[38], without strictly requiring specific conditions on the operator, whereas higher values lead to good reconstructions of extended targets. Consequently, the proposed approach has the advantage of allowing a correct retrieval of both sparse and non-sparse fault distributions, provided that a proper choice of the norm exponent is performed.

The developed approach is validated by means of numerical simulations concerning both simplified and realistic arrays. In particular, two different failure distributions have been analyzed: (a) damaged elements randomly selected from a uniform distribution, and (b) failures with normal distribution around a certain location. Thus, the case in which failures are spread all over the surface, as well as the one with clustered damages, have been considered and tested [39]–[41].

The paper is organized as follows. The mathematical formulation of the developed approach is discussed in Section II, whereas in Section III numerical results are provided and discussed. Lastly, conclusions are reported in Section IV.

II. METHODS AND PROCEDURES

The antenna configuration considered in this paper is shown in Fig. 1. A planar array composed by N elements placed at positions (x_n, y_n) and with excitations weights c_n, $n = 1, .., N$, is assumed. The electric field radiated by the AUT is collected in the far-field region on a hemispherical surface along M directions (θ_m, ϕ_m), $\theta \in [0°, 90°]$, $\phi \in [0°, 360°)$ with sampling step $\Delta\theta = \Delta\phi$. Under such a configuration, the antenna diagnostics problem can be stated as follows: given the set of measurements of the field radiated by the AUT, identify the possibly present faulty elements.

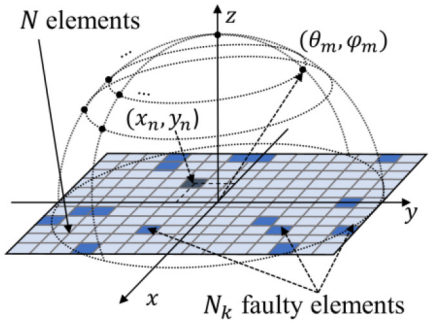

FIGURE 1. Geometry of the planar array diagnosis problem.

A. ARRAY RADIATION MODEL

As it is well known, the field radiated by an antenna array in the far-field region depends upon the geometry and the excitations weights c_n of its elements. In details, the far-field radiation pattern of the ideal reference array (i.e., without failures) in the direction (θ_m, ϕ_m) is given by [42], [43]

$$\begin{aligned}\mathbf{E}(\theta_m, \varphi_m) &= E_\theta(\theta_m, \phi_m)\widehat{\boldsymbol{\theta}} + E_\phi(\theta_m, \phi_m)\widehat{\boldsymbol{\phi}} \\ &= \sum_{n=1}^{N} c_n \mathbf{P}_n(\theta_m, \phi_m) e^{j\frac{2\pi}{\lambda}(x_n \sin\theta_m \cos\phi_m + y_n \sin\theta_m \sin\phi_m)}\end{aligned} \tag{1}$$

where λ is the wavelength in free space at the working angular frequency ω_{PA} and $\mathbf{P}_n(\theta_m, \phi_m) = P_{n\theta}(\theta_m, \phi_m)\widehat{\boldsymbol{\theta}} + P_{n\phi}(\theta_m, \phi_m)\widehat{\boldsymbol{\phi}}$ is the embedded pattern of nth element along the mth direction. In particular, $\mathbf{P}_n(\theta_m, \phi_m)$ represents the far-field pattern produced by the array when the nth element is excited (with $c_n = 1$) whereas all the other elements have $c_l = 0$ for $l \neq n$ with $l = 1, \ldots, N$ and are terminated with matched loads [33], [42], [44]. In such a way, the embedded pattern takes into account not only the single element structure but also the possible couplings between the elements, enabling a correct representation of the radiated far-field even in the case of real antennas [45], [46].

By combining all the M directions, the following linear systems (one for each polarization) are obtained:

$$\underline{e}_{\theta/\phi} = [H]_{\theta/\phi}\underline{c} \tag{2}$$

where

$$\underline{e}_{\theta/\phi} \triangleq \begin{bmatrix} E_{\theta/\phi}(\theta_1, \phi_1) \\ E_{\theta/\phi}(\theta_2, \phi_2) \\ \vdots \\ E_{\theta/\phi}(\theta_M, \phi_M) \end{bmatrix}, \quad \underline{c} \triangleq \begin{bmatrix} c_1 \\ c_2 \\ \vdots \\ c_N \end{bmatrix} \tag{3}$$

and $[H]_{\theta/\phi}$ is a $M \times N$ matrix whose elements are given by

$$\left\{[H]_{\theta/\phi}\right\}_{mn} \triangleq P_{n\theta/\phi}(\theta_m, \phi_m) e^{j\frac{2\pi}{\lambda}(x_n \sin\theta_m \cos\phi_m + y_n \sin\theta_m \sin\phi_m)} \tag{4}$$

As regards the AUT, it is assumed that a subset of $N_k = kN$ array elements is damaged, k being the failure rate. Consequently, the AUT excitation vector $\hat{\underline{c}}$ is in general different from the ideal one $\underline{c}$, and can be expressed as

$$\hat{c}_n = \nu_n c_n \tag{5}$$

where $\nu_n \in [0, 1]$. In particular, $\nu_n = 1$ for the correctly working elements, and $\nu_n < 1$ for the faulty elements.

The array excitation vector $\hat{\underline{c}}$ is related to far-field measurements, $\hat{\underline{e}}$, by equations similar to (2), i.e.,

$$\hat{\underline{e}}_{\theta/\phi} = [H]_{\theta/\phi} \hat{\underline{c}} \tag{6}$$

As usually done in the literature [31], [33], [34], in this work it is assumed to have at our disposal both the far-field measurements due to the ideal reference array and to the AUT. Under this assumption, the failure vector, $\underline{\Delta c} = \underline{c} - \widehat{\underline{c}}$ can be related to the differential samples of the radiated field, $\underline{\Delta e}_{\theta/\phi} = \underline{e}_{\theta/\phi} - \hat{\underline{e}}_{\theta/\phi}$, by means of the following linear model:

$$\underline{\Delta e}_{\theta/\phi} = [H]_{\theta/\phi} \underline{\Delta c} \tag{7}$$

If measurements of both components of the field are available, the inverse problem to be solved can be thus written as:

$$\underline{\Delta e} = \begin{bmatrix} \underline{\Delta e}_\theta \\ \underline{\Delta e}_\phi \end{bmatrix} = \begin{bmatrix} [H]_\theta \\ [H]_\phi \end{bmatrix} \underline{\Delta c} = [H] \underline{\Delta c} \tag{8}$$

In case only $\underline{\Delta e}_\theta$ or $\underline{\Delta e}_\phi$ is available, the inverse problem reduces to the solution of (7), i.e., $\underline{\Delta e} = \underline{\Delta e}_{\theta/\phi}$ and $[H] = [H]_{\theta/\phi}$ (by considering only the relevant polarization).

It is worth noting that $\underline{\Delta c}$ contains the differences among the excitations of the AUT and reference array (these latter being known by design). Consequently, the knowledge of such a quantity is sufficient to fully identify the faulty elements.

The solution strategy applied to invert (8) is outlined in the following Section.

B. INVERSION PROCEDURE

As it is well known, the inverse problem in (8) is strongly ill-posed; consequently, a regularized solving scheme needs to be adopted. To this end, in this paper the task of retrieving the AUT failure vector, $\underline{\Delta c}$, starting from the measurements of the radiated field is performed by using a truncated Landweber-like method in L^p spaces [36], [47]. In particular, the regularization is attained by means of an early truncation of the iterations. In this regard, it is assumed that the failure array and the differential measurement vectors belong to Lebesgue spaces, i.e., $\underline{\Delta c} \in X \subset L^p$ and $\underline{\Delta e} \in Y \subset L^p$. It is worth remarking that such an approach minimizes the cost functional $\Phi : X \to \mathbb{R}$ given by

$$\Phi(\underline{\Delta c}) = \frac{1}{2} \left\| [H] \underline{\Delta c} - \underline{\Delta e} \right\|_{L^p}^2 \tag{9}$$

where $\|\underline{r}\|_p = \left(\sum_{m=1}^{M} |r_m|^p\right)^{1/p}$ (with r_m the components of $\underline{r}$) denotes the norm of the functional space L^p [48] and $\underline{r} = [H]\underline{\Delta c} - \underline{\Delta e}$ is the residual vector. However, differently from standard Hilbert-space approaches, the minimization is performed in the dual space X^* of X, moving along nonstandard gradient directions that are different from the standard descent ones of classical Hilbert-space approaches. In this way, the regularization properties of the approach are enhanced by exploiting the different geometrical properties of the adopted Lebesgue spaces. Specifically, from an empirical point of view, it has been observed that low values of p (i.e., close to 1) are better suited for the reconstruction of sparse unknowns characterized by a low number of non-zero elements [37]. In such a way, the sparsity of the solution can be promoted without requiring specific sparsity conditions, e.g., that the RIP condition on the "measurement matrix", are satisfied [29], [34], [35], [49]. Conversely, higher values of p (i.e., close to 2) result in a stronger filtering and over-smoothing effect (as it often happens with Hilbert-space approaches), and are thus better suited for naturally smooth unknowns [37] . Clearly, if $p = 2$, that is X and Y are L^2 Hilbert spaces of square-integrable functions, the proposed approach reduces to a classical well-known least-squares minimization [36].

The steps of the developed algorithm can be summarized as follows:

1. Let $p > 1$ and $\underline{\Delta c}_0$ be a suitable starting guess (a null vector $\underline{\Delta c}_0 = 0$ is assumed if no a-priori information about defective elements is available)
2. Update the current solution performing the following steps.
   a. Map the current solution $\underline{\Delta c}_i$ and the residual vector $\underline{r}_i$ onto their dual spaces X^* and Y^*, i.e.,
   $$\begin{aligned} \underline{\Delta c}_i^* &= J_X\left(\underline{\Delta c}_i\right) \in X^* \\ \underline{r}_i^* &= J_Y\left(\underline{r}_i\right) \in Y^* \end{aligned} \tag{10}$$
   where J_X and J_Y are the duality maps of the considered Lebesgue spaces X and Y. In particular, J_X is defined as [50]
   $$J_X\left(\underline{x}\right) = \left\|\underline{x}\right\|_p^{2-p} \begin{bmatrix} |x_1|^{p-1}\text{sign}(x_1) \\ \vdots \\ |x_N|^{p-1}\text{sign}(x_N) \end{bmatrix} \tag{11}$$
   and a similar relationship holds for J_Y.
   b. Compute the next solution candidate in the dual space as
   $$\underline{\Delta c}_{i+1}^* = \underline{\Delta c}_i^* - \alpha [H]^* \underline{r}_i^* \tag{12}$$
   where $[H]^*$ is the adjoint (i.e., the Hermitian transpose in the considered settings) of $[H]$.

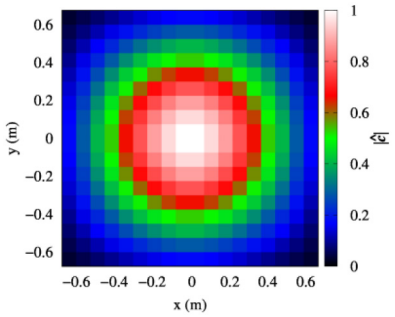

FIGURE 2. Magnitude of the reference excitation coefficients.

The step length α has been computed using the following empirical formula

$$\alpha = 0.25\left\{\|[H]\|_1^{-2} + (p-1)\left(\|[H]\|_2^{-2} - \|[H]\|_1^{-2}\right)\right\} \tag{13}$$

c. Retrieve the solution in the original space X, i.e.,

$$\underline{\Delta c}_{i+1} = J_{X^*}\left(\underline{\Delta c}^*_{i+1}\right) \tag{14}$$

where the duality map is computed as in (10) by replacing p with its Holder conjugate $p^* = p/(p-1)$ [50].

3. Iterate step 2. for $i = 0, 1, \ldots, L$, or until a predefined convergence criterion is satisfied.

III. NUMERICAL RESULTS

The antenna diagnostics technique described in the previous Section has been validated through a set of numerical simulations, involving both ideal arrays (i.e., composed by isotropic elements) and realistic structures. In all cases, the reference excitations are given by a Taylor one-parameter current distribution [51]. The sidelobe level of Taylor array has been set to $R = 25$ dB.

A. IDEAL ARRAY

A planar array of N ideal isotropic elements with $\lambda/2$ spacing ($f = 2$ GHz) is considered. Fig. 2 shows the magnitude of reference excitations of a planar array with $N = N_x \times N_y = 18 \times 18 = 324$ elements.

In order to perform the diagnosis, at first, the reference array without faulty elements has been simulated. Then, a second simulation has been performed considering the array with faulty elements. Afterwards, a white Gaussian noise having zero-mean value and a signal-to-noise ratio $SNR = 25$ dB has been added to the data in order to corrupt them and simulate noisy measurements. In this way, by subtracting the measurements in the far-field region produced by the ideal reference array, the differential samples $\underline{\Delta e}$ have been obtained. In particular, the simulated measurements have been collected in the far-field region along M directions (θ_m, ϕ_m), $\theta \in [0°, 90°]$, $\phi \in [0°, 360°)$ with sampling step $\Delta\theta = \Delta\phi = 10°$. Consequently, $M = 325$ data

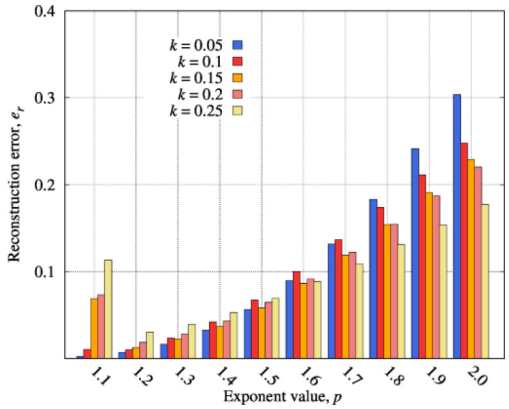

FIGURE 3. Normalized mean square reconstruction error by varying the exponent parameter p with failure rate $k \in [0.05, 0.25]$. Uniformly distributed failures.

are provided in input to the proposed method to diagnose the possibly faulty elements of the antenna array.

Concerning the failure configurations, two different types of distributions of faulty elements have been considered. In the first one, discussed in sub-section 1), the faulty elements are randomly distributed in the whole array, thus leading to failures that are sparse all over the array. In the second case, described in sub-section 2), clustered failures are considered, i.e., the faulty elements are localized in a given region of the array. In both cases, different failure rates $k \in [0.05, 0.25]$ have been analyzed, by randomly generating a configuration with total failures (i.e., characterized by $v_n = 0$).

In order to evaluate the accuracy of the results, the following normalized mean square reconstruction error has been used [31], [39]:

$$e_r = \frac{\left\|\underline{\Delta c}_{act} - \underline{\Delta \tilde{c}}\right\|_2^2}{\left\|\underline{\Delta c}_{act}\right\|_2^2} \tag{15}$$

where $\underline{\Delta \tilde{c}}$ and $\underline{\Delta c}_{act}$ are the reconstructed and actual failure vectors.

1) UNIFORMLY DISTRIBUTED FAILURES

A first analysis has been carried out considering an array with randomly distributed faults over the whole antenna aperture. In order to assess the performance of this technique, different rates of failing elements have been considered. In details, the failure rate in the AUT, k, has been varied from 0.05 to 0.25 and the value of v_n defined in (5) has been set $v_n = 0$ for each faulty element, i.e., total failures have been considered. As regards the method parameters, a sweep on the exponent parameter p between 1.1 and 2.0, for each different failure rate k, has been carried out. Fig. 3 shows the relative reconstruction errors on the excitations versus the parameter p with $k \in [0.05, 0.25]$. As can be noticed, except for the cases $k = \{0.05, 0.1\}$, in which the relative reconstruction error, e_r, monotonically increases versus p and is smaller in the lower bound $p = 1.1$, for all the other failure rate cases, the error has a minimum for $p = 1.2$, and then it goes up

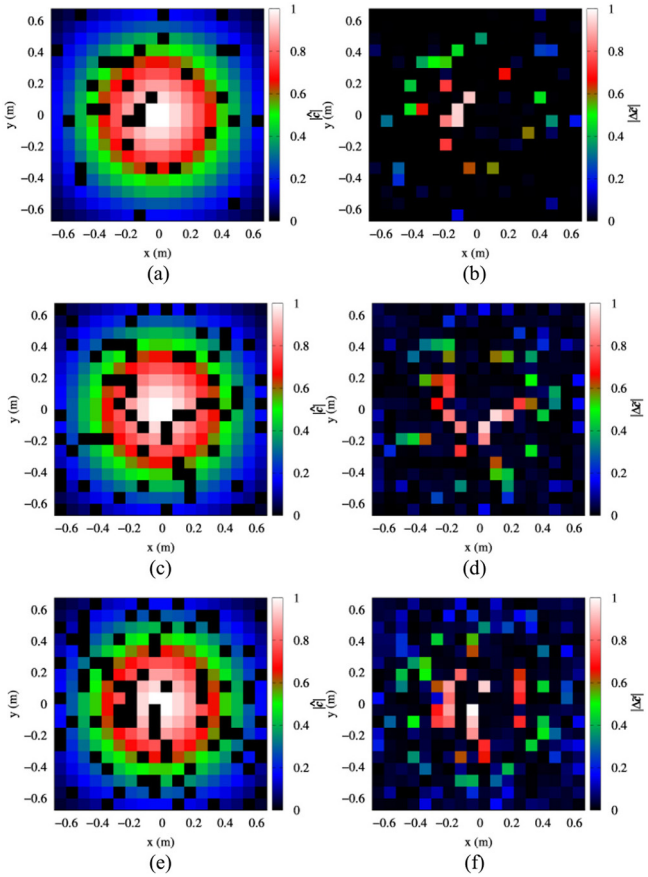

FIGURE 4. Magnitude of the excitations of the antenna under test with failure rate (a) $k = 0.1$, (c) $k = 0.2$, (e) $k = 0.25$. Magnitude of the best reconstructed failure vector elements with (b) $k = 0.1$, (d) $k = 0.2$ and (f) $k = 0.25$. Uniformly distributed failures.

again with greater values of p. In particular, as expected, low values of p, close to 1, are beneficial in recovering very sparse unknowns with a small number of non-zero elements, whereas higher values of p may improve the estimation when several non-zero elements of the unknown vector are present. By increasing the failure rate, the unknowns are less and less sparse; therefore, the optimum p slightly increases (although it always remains significantly lower than 2). Moreover, it is worth noting that for medium-high p the error decreases as the failure rate increases, vice versa for low values of p, the opposite trend can be observed. Thus, the value $p = 1.2$ represent a good trade-off since the method provides good reconstruction results for different failure rates.

The magnitude of the reconstructed excitation vector obtained using the optimal values of the norm parameter p for some values of the failure rate are shown in Fig. 4(b) ($k = 0.1$, $p = 1.1$), Fig. 4(d) ($k = 0.2$, $p = 1.2$), and Fig. 4(f) ($k = 0.25$, $p = 1.2$). The corresponding actual distributions are reported in Fig. 4(a), Fig. 4(c) and Fig. 4(e). In all cases, a very good estimation can be observed.

In this initial set of simulations, the number of iterations has been set to the value L^* providing the minimum normalized mean square error. In order to better analyze the convergence of the method, the trend of the normalized residualΦ_N and of the error e_r versus the number of iterations has been studied. In particular, Fig. 5 shows the graphs of the residual and error versus the number of iterations $L \in [1, 10000]$ with a failure rate of 0.1 [Fig. 5(a) and Fig. 5(d)], 0.15 [Fig. 5(b) and Fig. 5(e)], and 0.25 [Fig. 5(c) and Fig. 5(f)], for the best exponent parameters $p = 1.1,1.2$, respectively. As a reference case, the results obtained considering the conventional inversion in Hilbert spaces (i.e., with $p = 2$) are also provided.

In all the reported cases, the semiconvergence behavior of the reconstruction error e_r, which characterizes any iterative regularization method, is clearly visible. Semiconvergence means that the first iterations provide a good noise filtering, and consequently the accuracy of the solution $\underline{\Delta c_i}$ improves, while the subsequent ones restore from data components with higher noise, so that the accuracy starts to become worse. It is worth highlighting that semiconvergence holds for the reconstruction error e_r only, not for the residual $\Phi(\underline{\Delta c_i})$. In fact, the normalized residual [Fig. 5(a-c)] always decreases, whereas the errors [Fig. 5 (d-f)] decrease until a minimum value is reached (at the optimal iteration number L^*) and then start to rise. For this reason, the number of iteration plays the role of regularizing parameter. In particular, when the optimal norm parameter is considered, a fast-converging phase can be observed, followed by a steep ascending trend. In the Hilbert-space cases ($p = 2$), after an initial fast decrease, the error curves tend to flatten, and after reaching the minimum values undergo a steeper increase. The corresponding normalized residual [Fig. 5(a-c)], when considering the optimal values of p, tends to flatten out near the optimum value of iterations L^*. Instead, for the Hilbert-space case, the residual exhibits a plateau approximately corresponding to the flat part of the error curve. It is also worth noting that the error obtained with the optimal values of p is always significantly lower than the corresponding results provided by conventional Hilbert-space approaches. Moreover, as expected, the difference between the errors is higher for the lower failure rate and decreases when k increases, since a lower sparsity is present.

As concerns the computational burden, II reports the times required to perform the inversion on a personal computer equipped with an Intel Core i7-11700F CPU at 2.50 GHz and 16 GB of RAM,

2) CLUSTERED FAILURES

In this section, a second analysis is presented considering an array with clustered faulty elements. Indeed, faults may be generated by several phenomena, such as damages in the array feed networks, mechanical and manufacturing errors, and presence of deposit of particles on arrays (e.g., dust or snow) [39], [52]–[54], and may be thus mainly localized in a region of the array. In this case, random faulty elements have been generated according to a normal distribution with standard deviation $\sigma_x = k(N_x/3)$, $\sigma_y = k(N_y/3)$, and mean

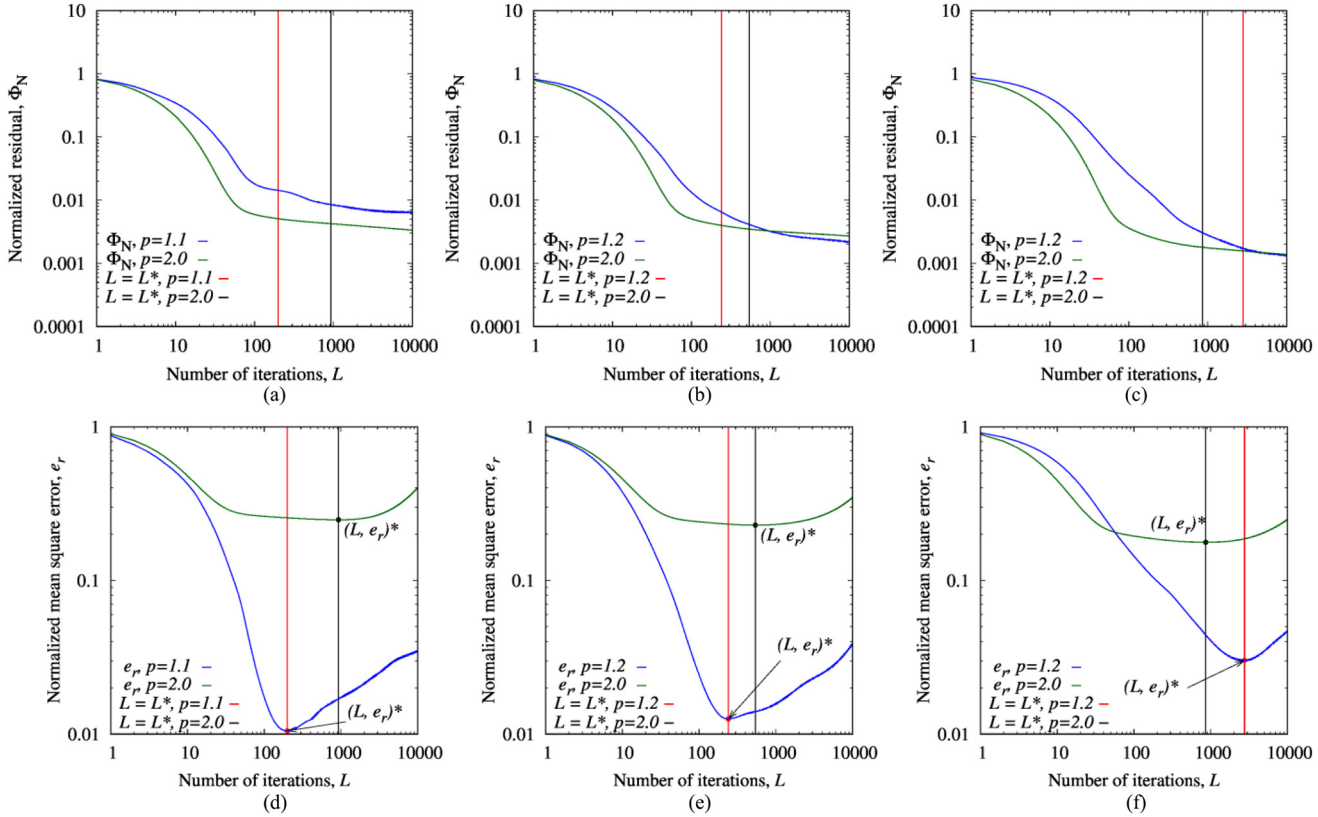

FIGURE 5. Normalized residual with failure rate (a) $k = 0.1$ and $p = \{1.1,\ 2.0\}$, (b) $k = 0.15$ and $p = \{1.2,\ 2.0\}$, (c) $k = 0.25$ and $p = \{1.2,\ 2.0\}$. Normalized mean square error with failure rate (d) $k = 0.1$ and $p = \{1.1,\ 2.0\}$, (e) $k = 0.15$ and $p = \{1.2,\ 2.0\}$, (f) $k = 0.25$ and $p = \{1.2,\ 2.0\}$. Uniformly distributed failures.

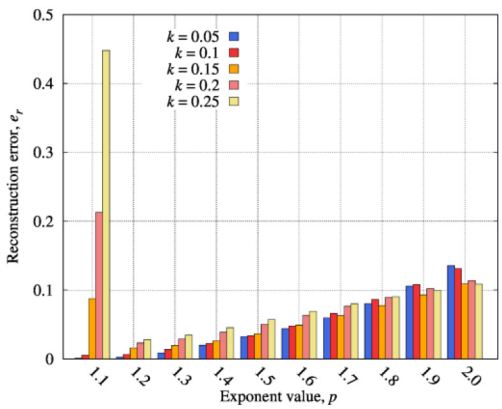

FIGURE 6. Normalized mean square reconstruction error by varying the exponent parameter p with failure rate $k \in [0.05, 0.25]$. Clustered failures.

TABLE 1. Computational times.

	Failure rate	Time (s)
Uniformly distributed failures	0.05	0.207
	0.1	0.520
	0.15	0.887
	0.2	4.786
	0.25	9.414
Clustered failures	0.05	0.275
	0.1	0.480
	0.15	3.884
	0.2	8.215
	0.25	17.449

$\mu_x = N_x/3, \mu_y = N_y/2$. As in Section III-A1), the failure rate in the AUT, k, has been varied from 0.05 to 0.25, and, for each case, a random configuration with total failures have been taken into account (i.e., in (5), $v_n = 0$ is assumed). The method has been studied by changing the exponent parameter p between 1.1 and 2.0 for each different failure rate k. The iterations are stopped at the optimal iteration providing the minimum error. Fig. 6 shows the relative reconstruction error versus the exponent value p for the considered values of the failure rate k. The behavior is similar to the one observed in Section III-A1). For $k = \{0.05,\ 0.1\}$ the trend of the error is growing monotonically, whereas for higher values it has a minimum in $p = 1.2$. Moreover, the error for $p > 1.3$ versus k is smaller compared with those reported in Fig. 3. This is motivated by the different nature of the unknown vector: here, the failures are mainly concentrated in a particular region of the array aperture. However, by comparing the trend of the error in Fig. 3 and in Fig. 6, it is worth noting that the error reaches the minimum for the same value of exponent p in both two cases for given failure rate, and the best exponent parameter p is always inside the range $p \in [1.1, 1.2]$. Fig. 7 shows the best reconstructed excitation vectors, for $k = 0.1$ [Fig. 7(b) and $p = 1.1$], $k = 0.2$ [Fig. 7(d) and $p = 1.2$] and $k = 0.3$ [Fig. 7(f)

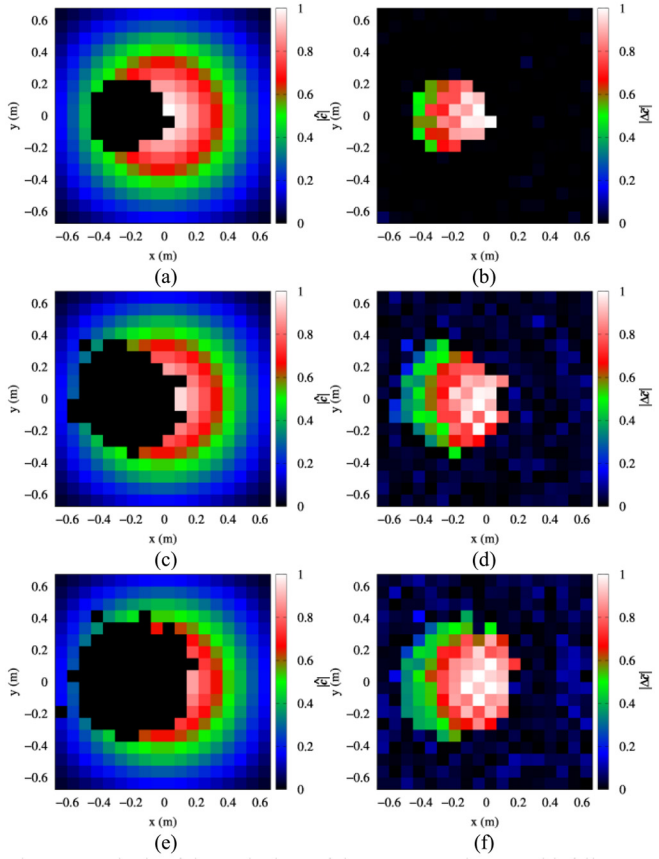

FIGURE 7. Magnitude of the excitations of the antenna under test with failure rate (a) $k = 0.1$, (c) $k = 0.2$ and (e) $k = 0.25$. Magnitude of the best reconstructed failure vector elements with (b) $k = 0.1$, (d) $k = 0.2$ and (f) $k = 0.25$. Clustered failures.

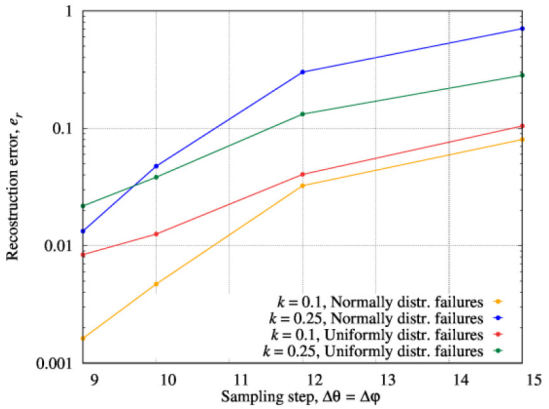

FIGURE 8. Normalized mean square reconstruction error with failure rate $k \in \{0.1, 0.25\}$ by varying the sampling gap $\Delta\theta = \Delta\varphi \in [9°, 15°]$.

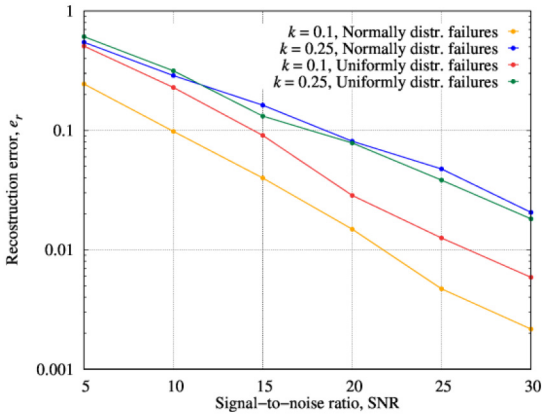

FIGURE 9. Normalized mean square reconstruction error with failure rate $k \in \{0.1, 0.25\}$ by varying the signal-to-noise ratio SNR$\in$ [5, 30] dB.

and $p = 1.2$], compared with the actual excitations of the antenna under test. A good estimation has been obtained for all the three reconstructions. For completeness, I reports the computational times required for the inversion.

B. VARIATION OF NUMBER OF MEASUREMENT POINTS

In order to estimate the behavior of the method versus the number of measurements, a set of tests has been performed by varying the sampling gap $\Delta\theta = \Delta\varphi$. This analysis has been conducted for the two different kinds of distribution: uniform and normal ones. The configuration is the same used in the previous Sections and $k = \{0.1,\ 0.25\}$ has been considered for $\Delta\theta = \Delta\varphi = 9°$ ($M = 401$), $\Delta\theta = \Delta\varphi = 10°$ ($M = 325$), $\Delta\theta = \Delta\varphi = 12°$ ($M = 211$) and $\Delta\theta = \Delta\varphi = 15°$ ($M = 145$). As concerns method parameters, the exponent parameter has been set to the value $p = 1.2$. The trend of the reconstruction error on the excitations, e_r, is reported in Fig. 8. It is evident that in all scenarios the best reconstruction result occurs with a higher number of available measurements ($e_r < 0.05$ for the four analyzed cases and $\Delta\theta = \Delta\varphi = 9°$). Indeed, the error monotonically increases by growing the sampling gap and with $\Delta\theta = \Delta\varphi = 15°$ the number of measurements is not sufficient to suitably retrieve the excitations in all the analyzed distribution both for $k = 0.1$ and $k = 0.25$.

Therefore, on the one hand, with a smaller number of measurements, the input information decreases, and the reconstruction error increases. However, on the other hand, with low values of $\Delta\theta = \Delta\varphi$, the reconstruction is accurate, but the measurement procedure is more demanding since a high number of field data is required. This way, with $\Delta\theta = \Delta\varphi = 10°$, a good trade-off between number of measurements and estimation can be attained. Such a value of sampling gap, $\Delta\theta = \Delta\varphi = 10°$, is also in agreement with the number of degrees of freedom of the radiated field that is $N_F = 324$ [55].

C. VARIATION OF SIGNAL-TO-NOISE RATIO

Subsequently, the effect on the performance of the level of noise introduced on data has been studied. In details, the SNR has been varied in the range SNR $\in [5, 30]$ dB with a step of 5 dB for both the distributions of faulty elements. The obtained results are summarized in Fig. 9. As expected, for both $k = \{0.1, 0.25\}$ and for the two different distributions of faults, the reconstruction error increases when SNR becomes lower. Specifically, from the trends of the error in Fig. 9,

TABLE 2. Normalized mean square reconstruction errors. Comparison with compressive sensing technique.

	Normalized mean square reconstruction error		
Failure rate	L1-Magic	L^p	Hilbertian space
0.05	0.0080	0.0006	0.1097
0.1	0.0131	0.0037	0.0993
0.15	0.0470	0.0153	0.1013
0.2	0.0622	0.0199	0.1158
0.25	0.1289	0.0339	0.1098

it can be observed that, for low SNR, the reconstruction accuracy gets worse and highly noisy data (SNR = 5 dB) do not allow the obtain a suitable reconstruction. Nevertheless, a SNR $\gtrsim$ 15 dB enables to achieve good reconstruction results by the proposed method in all the analyzed cases.

D. COMPARATIVE ASSESSMENT

In order to further assess the performance of the proposed method, a comparison with $L1$-norm compressive sensing techniques [34], which are widely used in antenna array diagnostics [29], [56], has been performed. In particular, the "L1-Magic" MATLAB package [57] with log-barrier algorithm has been used for solving the inverse problem in (8).

The ideal planar array of dimension $N = 18 \times 18 = 324$ used in the previous Sections has been adopted. $M = 325$ measurements collected with a sampling gap $\Delta\theta = \Delta\varphi = 10^\circ$ and $SNR = 25$ dB have been provided as input to both the developed procedure and the compressive sensing algorithm. Table 2 shows the normalized mean square errors for the case of clustered faulty elements and using failure rates $k = [0.05, 0.1, 0.15, 0.2, 0.25]$. In Table 2, the best recovery errors (achieved with $p = 1.1$ for $k = [0.05, 0.1]$ and with $p = 1.2$ for $k = [0.15, 0.2, 0.25]$) have been reported for the proposed method. Moreover, the errors obtained with classical Hilbert space approach are also given. As can be noticed, in all cases, the classical Hilbertian space method provides the worse results. Compared to the compressive sensing technique, the proposed approach enables a slightly better diagnostic accuracy especially when the failure rate increases. Indeed, although with low values of the failure rate (e.g., $k = 0.05$) both L^p and L1 approaches provide a quite good recovery error, when the failure rate increases and the unknown is less sparse, the recovery error of the proposed L^p scheme increases more slowly.

E. REALISTIC ARRAY

To evaluate the proposed approach in the presence of realistic arrays, a planar array of patch antennas with size $L_x = L_y = 622.1$ mm and $N_x = N_y = 10$ elements placed with spacing $\lambda_0/2$ ($f = 2.4$ GHz) has been considered. The patches have dimensions $W = H = 30.2$ mm and a dielectric substrate of thickness $l = 1.5$ mm characterized by a relative dielectric permittivity $\varepsilon_r = 4$ and dielectric loss tangent $\tan\delta = 0.015$ is located between the patches and the ground plane (perfect electric conductor). To feed each element, a lumped port is set between the patch and the ground plane

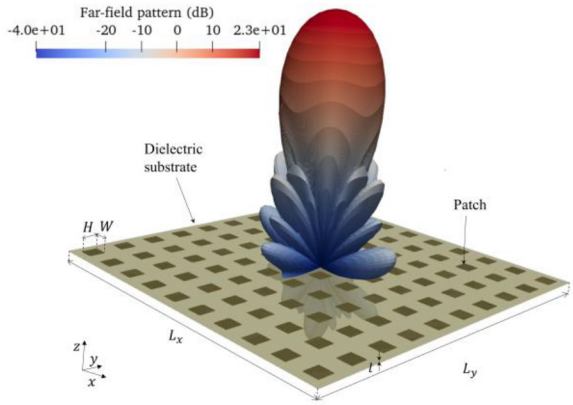

FIGURE 10. Planar array of patch antennas. Three-dimensional geometry and radiation pattern in logarithmic scale obtained with *openEMS* simulation.

with an offset along the y axis of -5.5 mm with respect to the patch center.

The FDTD open-source software *openEMS* has been used to simulate the antenna array and compute the radiated fields (those generated by reference and faulty antenna arrays and embedded patterns) [58], [59]. The simulations of antenna arrays have been performed with a domain of dimensions $647 \times 647 \times 25$ mm. Mur's absorbing conditions are imposed at boundaries [60]. A Gaussian modulated pulse with a band between 1.0 and 3.0 GHz has been used as excitation signal. A time step $\Delta t = 1.48 \times 10^{-12}$ s is considered, and $N_{array} = 1.85651 \times 10^6$ adaptive cubic cells have been used to discretize the simulation domain for computing the field of reference and faulty antenna arrays whereas a discretization of $N_{EP} = 1.43501 \times 10^6$ elements has been adopted to retrieve the embedded patterns. The failure rate in the AUT has been set to $k = 0.1$ and total failures have been considered (i.e., in (5), $\nu_n = 0$). Similar to the previous Section, at first the faults have been generated by considering a uniform random distribution over the array, and then by considering a normal distribution (to simulate clustered defective elements). As concerns the inversion method, the exponent parameter has been chosen to the value $p = 1.2$.

Fig. 10 shows the three-dimensional geometry and the radiation pattern of the reference antenna array. Moreover, Fig. 11(a) and Fig. 11(b) report the radiation pattern in the E-plane ($\varphi = 0^\circ$) and H-plane ($\varphi = 90^\circ$) both for reference and faulty antenna arrays ($k = 0.1$, $\nu_n = 0$ and uniformly distributed failures), respectively.

The θ- and φ-components of the electric far field are collected with angular steps $\Delta\theta = \Delta\varphi = 10^\circ$ in $M = 325$ points uniformly distributed on a hemisphere in the far-field region. Field data generated by AUT are corrupted with a white Gaussian noise having zero-mean value and a signal-to-noise ratio $SNR = 25$ dB.

The reconstructed magnitude of the feed coefficients of the elements compared with the actual excitations of the antenna under test for $k = 0.1$ with uniformly and normally distributed failures are shown in Fig. 12 and Fig. 13,

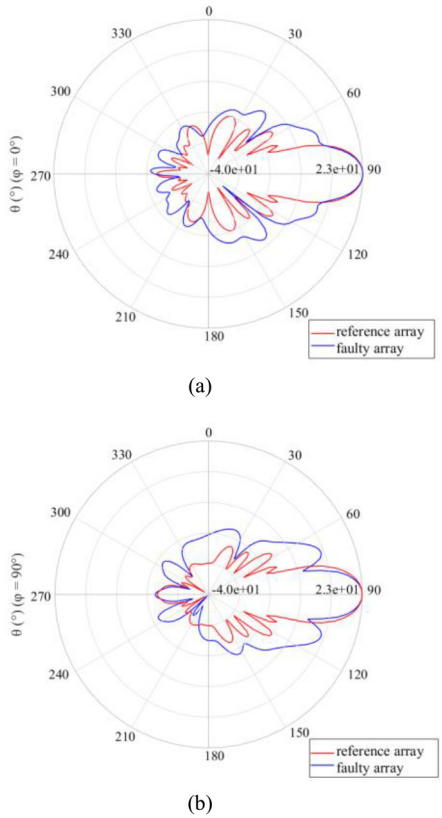

FIGURE 11. Far-field radiation pattern of reference and faulty array in the (a) E-plane ($\varphi = 0°$) and (b) H-plane ($\varphi = 90°$).

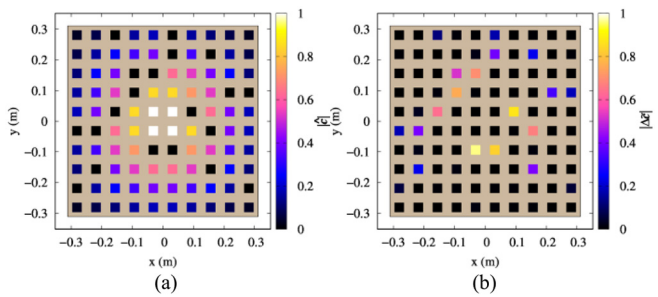

FIGURE 12. (a) Magnitude of the excitations of the antenna under test with failure rate $k = 0.1$. (b) Magnitude of the reconstructed failure vector elements with $k = 0.1$. Uniformly distributed failures.

respectively. As it can be noticed, a good diagnosis is achieved, since the failures are correctly localized, and their reconstruction is accurate in both cases. The obtained recovery error values are equal to $e_r = 0.007$ and $e_r = 0.0097$, respectively.

IV. CONCLUSION

In this paper, a novel approach for antenna array diagnosis has been presented. The aim of the proposed strategy is to retrieve the distribution of the faulty coefficients of the antenna under test by solving the underlying inverse problem. A Landweber-like scheme developed in the framework of L^p spaces has been proposed to find a regularized

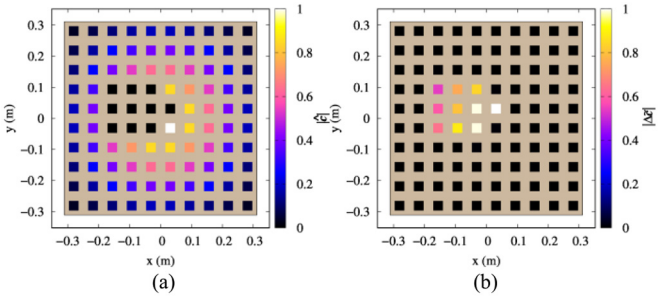

FIGURE 13. (a) Magnitude of the excitations of the antenna under test with failure rate $k = 0.1$. (b) Magnitude of the reconstructed failure vector elements with $k = 0.1$. Clustered failures.

solution of the inverse problem. The method has been validated through numerical simulations. In particular, a planar array configuration has been assumed with failures extracted from uniform and normal distributions. Moreover, different failure rates have been taken into consideration. Numerical results, which reveal the capability of retrieving diverse kinds of faulty elements distributions with different failure rates, show the effectiveness of the proposed diagnostics approach. Future studies will be devoted to including an extensive numerical assessment and testing the proposed approach in more complex scenarios.

REFERENCES

[1] R. L. Haupt and Y. Rahmat-Samii, "Antenna array developments: A perspective on the past, present and future," *IEEE Antennas Propag. Mag.*, vol. 57, no. 1, pp. 86–96, Feb. 2015, doi: 10.1109/MAP.2015.2397154.

[2] Y. Chen, W. Zhou, and S. Yang, "Design of a low-profile and low scattering wideband planar phased antenna array," *IEEE Trans. Antennas Propag.*, vol. 69, no. 12, pp. 8973–8978, Dec. 2021, doi: 10.1109/TAP.2021.3097099.

[3] O. M. Bucci, T. Isernia, S. Perna, and D. Pinchera, "Isophoric sparse arrays ensuring global coverage in satellite communications," *IEEE Trans. Antennas Propag.*, vol. 62, no. 4, pp. 1607–1618, Apr. 2014, doi: 10.1109/TAP.2013.2287901.

[4] Y. Yu, W. Hong, Z. H. Jiang, and H. Zhang, "A hybrid radar system with a phased transmitting array and a digital beamforming receiving array," *IEEE Trans. Antennas Propag.*, vol. 69, no. 4, pp. 1970–1981, Apr. 2021, doi: 10.1109/TAP.2020.3044368.

[5] M. Li *et al.*, "Machine learning in electromagnetics with applications to biomedical imaging: A review," *IEEE Antennas Propag. Mag.*, vol. 63, no. 3, pp. 39–51, Jun. 2021, doi: 10.1109/MAP.2020.3043469.

[6] E. Kim, C. T. Mohammadi, M. Asefi, J. Lovetri, I. Jeffrey, and C. Gilmore, "Imaging and calibration of electromagnetic inversion data with a single data set," *IEEE Open J. Antennas Propag.*, vol. 3, pp. 12–23, 2022, doi: 10.1109/OJAP.2021.3132100.

[7] J. A. T. Vasquez *et al.*, "Noninvasive inline food inspection via microwave imaging technology: An application example in the food industry," *IEEE Antennas Propag. Mag.*, vol. 62, no. 5, pp. 18–32, Oct. 2020, doi: 10.1109/MAP.2020.3012898.

[8] F. Foroutan and N. K. Nikolova, "UWB active antenna for microwave breast imaging sensing arrays," *IEEE Antennas Wireless Propag. Lett.*, vol. 18, no. 10, pp. 1951–1955, Oct. 2019, doi: 10.1109/LAWP.2019.2929016.

[9] A. Zeitler, J. Lanteri, C. Pichot, C. Migliaccio, P. Feil, and W. Menzel, "Folded reflectarrays with shaped beam pattern for foreign object debris detection on runways," *IEEE Trans. Antennas Propag.*, vol. 58, no. 9, pp. 3065–3068, Sep. 2010, doi: 10.1109/TAP.2010.2052564.

[10] R. J. Mailloux, "Array failure correction with a digitally beamformed array," *IEEE Trans. Antennas Propag.*, vol. 44, no. 12, pp. 1543–1550, Dec. 1996, doi: 10.1109/8.546240.

[11] G. Leone, M. A. Maisto, and R. Pierri, "Application of inverse source reconstruction to conformal antennas synthesis," *IEEE Trans. Antennas Propag.*, vol. 66, no. 3, pp. 1436–1445, Mar. 2018, doi: 10.1109/TAP.2018.2794397.

[12] G. Leone, F. Munno, and R. Pierri, "Inverse source on conformal conic geometries," *IEEE Trans. Antennas Propag.*, vol. 69, no. 3, pp. 1596–1609, Mar. 2021, doi: 10.1109/TAP.2020.3016375.

[13] J. J. Lee, E. M. Ferren, D. P. Woollen, and K. M. Lee, "Near-field probe used as a diagnostic tool to locate defective elements in an array antenna," *IEEE Trans. Antennas Propag.*, vol. 36, no. 6, pp. 884–889, Jun. 1988, doi: 10.1109/8.1192.

[14] L. Gattoufi, D. Picard, A. Rekiouak, and J. C. Bolomey, "Matrix method for near-field diagnostic techniques of phased arrays," in *Proc. Int. Symp. Phased Array Syst. Technol.*, Oct. 1996, pp. 52–57, doi: 10.1109/PAST.1996.565934.

[15] O. M. Bucci, M. D. Migliore, G. Panariello, and P. Sgambato, "Accurate diagnosis of conformal arrays from near-field data using the matrix method," *IEEE Trans. Antennas Propag.*, vol. 53, no. 3, pp. 1114–1120, Mar. 2005, doi: 10.1109/TAP.2004.842656.

[16] A. Patnaik, B. Choudhury, P. Pradhan, R. K. Mishra, and C. Christodoulou, "An ANN application for fault finding in antenna arrays," *IEEE Trans. Antennas Propag.*, vol. 55, no. 3, pp. 775–777, Mar. 2007, doi: 10.1109/TAP.2007.891557.

[17] A. Buonanno, M. D'Urso, M. Cicolani, and S. Mosca, "Large phased arrays diagnostic via distributional approach," *Progr. Electromagn. Res.*, vol. 92, pp. 153–166, May 2009, doi: 10.2528/PIER09031704.

[18] Q. Li, K. Dai, X. Wang, Y. Zhang, H. Zhang, and D. Jiang, "Low-complexity failed element diagnosis for radar-communication mmwave antenna array with low SNR," *Electronics*, vol. 8, no. 8, p. 8, Aug. 2019, doi: 10.3390/electronics8080904.

[19] K. Konno, S. Asano, T. Umenai, and Q. Chen, "Diagnosis of array antennas using eigenmode currents and near-field data," *IEEE Trans. Antennas Propag.*, vol. 66, no. 11, pp. 5982–5989, Nov. 2018, doi: 10.1109/TAP.2018.2866544.

[20] G. Álvarez-Narciandi, J. Laviada, Y. Álvarez-López, and F. Las-Heras, "Portable freehand system for real-time antenna diagnosis and characterization," *IEEE Trans. Antennas Propag.*, vol. 68, no. 7, pp. 5636–5645, Jul. 2020, doi: 10.1109/TAP.2020.2978936.

[21] J. L. A. Quijano and G. Vecchi, "Improved-accuracy source reconstruction on arbitrary 3-D surfaces," *IEEE Antennas Wireless Propag. Lett.*, vol. 8, pp. 1046–1049, 2009, doi: 10.1109/LAWP.2009.2031988.

[22] T. Brown, I. Jeffrey, and P. Mojabi, "Multiplicatively regularized source reconstruction method for phaseless planar near-field antenna measurements," *IEEE Trans. Antennas Propag.*, vol. 65, no. 4, pp. 2020–2031, Apr. 2017, doi: 10.1109/TAP.2017.2670518.

[23] T. F. Eibert and C. H. Schmidt, "Multilevel fast multipole accelerated inverse equivalent current method employing Rao–Wilton–Glisson discretization of electric and magnetic surface currents," *IEEE Trans. Antennas Propag.*, vol. 57, no. 4, pp. 1178–1185, Apr. 2009, doi: 10.1109/TAP.2009.2015828.

[24] M. T. Bevacqua, L. Crocco, L. D. Donato, and T. Isernia, "Non-linear inverse scattering via sparsity regularized contrast source inversion," *IEEE Trans. Comput. Imag.*, vol. 3, no. 2, pp. 296–304, Jun. 2017, doi: 10.1109/TCI.2017.2675708.

[25] M. Ambrosanio and V. Pascazio, "A compressive-sensing-based approach for the detection and characterization of buried objects," *IEEE J. Sel. Topics Appl. Earth Observ. Remote Sens.*, vol. 8, no. 7, pp. 3386–3395, Jul. 2015, doi: 10.1109/JSTARS.2015.2421812.

[26] Q. Wu, Z. Lai, and M. G. Amin, "Through-the-wall radar imaging based on bayesian compressive sensing exploiting multipath and target structure," *IEEE Trans. Comput. Imag.*, vol. 7, pp. 422–435, 2021, doi: 10.1109/TCI.2021.3071957.

[27] M. T. Bevacqua and R. Scapaticci, "A compressive sensing approach for 3D breast cancer microwave imaging with magnetic nanoparticles as contrast agent," *IEEE Trans. Med. Imag.*, vol. 35, no. 2, pp. 665–673, Feb. 2016, doi: 10.1109/TMI.2015.2490340.

[28] R. Palmeri, M. T. Bevacqua, L. Crocco, T. Isernia, and L. Di Donato, "Microwave imaging via distorted iterated virtual experiments," *IEEE Trans. Antennas Propag.*, vol. 65, no. 2, pp. 829–838, Feb. 2017, doi: 10.1109/TAP.2016.2633070.

[29] A. Massa, P. Rocca, and G. Oliveri, "Compressive sensing in electromagnetics—A review," *IEEE Antennas Propag. Mag.*, vol. 57, no. 1, pp. 224–238, Feb. 2015, doi: 10.1109/MAP.2015.2397092.

[30] B. Fuchs, L. L. Coq, and M. D. Migliore, "Fast antenna array diagnosis from a small number of far-field measurements," *IEEE Trans. Antennas Propag.*, vol. 64, no. 6, pp. 2227–2235, Jun. 2016, doi: 10.1109/TAP.2016.2547023.

[31] R. Palmeri, T. Isernia, and A. F. Morabito, "Diagnosis of planar arrays through phaseless measurements and sparsity promotion," *IEEE Antennas Wireless Propag. Lett.*, vol. 18, no. 6, pp. 1273–1277, Jun. 2019, doi: 10.1109/LAWP.2019.2914529.

[32] T. Ince and G. Ögücü, "Array failure diagnosis using nonconvex compressed sensing," *IEEE Antennas Wireless Propag. Lett.*, vol. 15, pp. 992–995, 2016, doi: 10.1109/LAWP.2015.2489760.

[33] M. Salucci, A. Gelmini, G. Oliveri, and A. Massa, "Planar array diagnosis by means of an advanced Bayesian compressive processing," *IEEE Trans. Antennas Propag.*, vol. 66, no. 11, pp. 5892–5906, Nov. 2018, doi: 10.1109/TAP.2018.2866534.

[34] M. D. Migliore, "Array diagnosis from far-field data using the theory of random partial fourier matrices," *IEEE Antennas Wireless Propag. Lett.*, vol. 12, pp. 745–748, 2013, doi: 10.1109/LAWP.2013.2270931.

[35] M. E. Tipping, "Sparse Bayesian learning and the relevance vector machine," *J. Mach. Learn. Res.*, vol. 1, pp. 211–244, Jun. 2001.

[36] C. Estatico, M. Pastorino, and A. Randazzo, "A novel microwave imaging approach based on regularization in Lp Banach spaces," *IEEE Trans. Antennas Propag.*, vol. 60, no. 7, pp. 3373–3381, Jul. 2012, doi: 10.1109/TAP.2012.2196925.

[37] C. Estatico, A. Fedeli, M. Pastorino, and A. Randazzo, "Microwave imaging of elliptically shaped dielectric cylinders by means of an LP banach-space inversion algorithm," *Meas. Sci. Technol.*, vol. 24, no. 7, Jul. 2013, Art. no. 074017, doi: 10.1088/0957-0233/24/7/074017.

[38] C. Estatico, A. Fedeli, M. Pastorino, A. Randazzo, and E. Tavanti, "A phaseless microwave imaging approach based on a lebesgue-space inversion algorithm," *IEEE Trans. Antennas Propag.*, vol. 68, no. 12, pp. 8091–8103, Dec. 2020, doi: 10.1109/TAP.2020.2999789.

[39] M. E. Eltayeb, T. Al-Naffouri, and R. W. Heath, "Compressive sensing for millimeter wave antenna array diagnosis," *IEEE Trans. Commun.*, vol. 66, no. 6, pp. 2708–2721, Jun. 2018, doi: 10.1109/TCOMM.2018.2790403.

[40] J. R. Mohammed, A. J. Abdulqader, and R. H. Thaher, "Array pattern recovery under amplitude excitation errors using clustered elements," *Prog. Electromagn. Res. M*, vol. 98, pp. 183–192, Jan. 2020, doi: 10.2528/PIERM20101906.

[41] S. Frache, M. Graziano, and M. Zamboni, "A flexible simulation methodology and tool for nanoarray-based architectures," in *Proc. Int. Conf. Comput. Design*, Oct. 2010, pp. 60–67. doi: 10.1109/ICCD.2010.5647586.

[42] D. F. Kelley and W. L. Stutzman, "Array antenna pattern modeling methods that include mutual coupling effects," *IEEE Trans. Antennas Propag.*, vol. 41, no. 12, pp. 1625–1632, Dec. 1993, doi: 10.1109/8.273305.

[43] C. A. Balanis, *Antenna Theory: Analysis and Design*, 4th ed. Hoboken, NJ, USA: Wiley, 2016.

[44] H. M. Aumann, A. J. Fenn, and F. G. Willwerth, "Phased array antenna calibration and pattern prediction using mutual coupling measurements," *IEEE Trans. Antennas Propag.*, vol. 37, no. 7, pp. 844–850, Jul. 1989, doi: 10.1109/8.29378.

[45] D. M. Pozar, "The active element pattern," *IEEE Trans. Antennas Propag.*, vol. 42, no. 8, pp. 1176–1178, Aug. 1994, doi: 10.1109/8.310010.

[46] S. Fofana, B. Fuchs, S. Avrillon, F. Colombel, L. Lézé, and S. Palud, "Reconfigurable antenna array with reduced power consumption—Synthesis methods and experimental validations in S-band," *IEEE Trans. Antennas Propag.*, vol. 69, no. 4, pp. 2023–2030, Apr. 2021, doi: 10.1109/TAP.2020.3026888.

[47] P. Brianzi, F. Di Benedetto, and C. Estatico, "Improvement of space-invariant image deblurring by preconditioned landweber iterations," *SIAM J. Sci. Comput.*, vol. 30, no. 3, pp. 1430–1458, Jan. 2008, doi: 10.1137/050636024.

[48] O. Scherzer, M. Grasmair, H. Grossauer, M. Haltmeier, and F. Lenzen, *Variational Methods in Imaging*. New York, NY, USA: Springer, 2009, doi: 10.1007/978-0-387-69277-7.

[49] G. Oliveri, M. Salucci, N. Anselmi, and A. Massa, "Compressive sensing as applied to inverse problems for imaging: Theory, applications, current trends, and open challenges," *IEEE Antennas Propag. Mag.*, vol. 59, no. 5, pp. 34–46, Oct. 2017, doi: 10.1109/MAP.2017.2731204.

[50] T. Schuster, B. Kaltenbacher, B. Hofmann, and K. S. Kazimierski, *Regularization Methods in Banach Spaces*. Berlin, Germany: De Gruyter, 2012, doi: 10.1515/9783110255720.
[51] S. J. Orfanidis. "Electromagnetic waves and antennas." 2016. [Online]. Available: http://www.ece.rutgers.edu/∼orfanidi/ewa/
[52] A. Zahedi and B. A. Arand, "GA-based approach to phase compensation of large phased array antennas," *J. Syst. Eng. Electron.*, vol. 29, no. 4, pp. 723–730, Aug. 2018, doi: 10.21629/JSEE.2018.04.07.
[53] F. Harrou and Y. Sun, "Statistical monitoring of linear antenna arrays," *Eng. Sci. Technol. Int. J.*, vol. 19, no. 4, pp. 1781–1787, Nov. 2016, doi: 10.1016/j.jestch.2016.10.010.
[54] P. Rocca, L. Manica, N. Anselmi, and A. Massa, "Analysis of the pattern tolerances in linear arrays with arbitrary amplitude errors," *IEEE Antennas Wireless Propag. Lett.*, vol. 12, pp. 639–642, 2013, doi: 10.1109/LAWP.2013.2261912.
[55] O. M. Bucci, C. Gennarelli, and C. Savarese, "Representation of electromagnetic fields over arbitrary surfaces by a finite and nonredundant number of samples," *IEEE Trans. Antennas Propag.*, vol. 46, no. 3, pp. 351–359, Mar. 1998, doi: 10.1109/8.662654.
[56] M. D. Migliore, "A compressed sensing approach for array diagnosis from a small set of near-field measurements," *IEEE Trans. Antennas Propag.*, vol. 59, no. 6, pp. 2127–2133, Jun. 2011, doi: 10.1109/TAP.2011.2144556.
[57] E. Candes and J. Romberg, "L1-MAGIC: Recovery of sparse signals via convex programming," Oct. 2005. [Online]. Available: https://candes.su.domains/software/l1magic/downloads/l1magic.pdf
[58] T. Liebig, A. Rennings, S. Held, and D. Erni, "openEMS—A free and open source equivalent-circuit (EC) FDTD simulation platform supporting cylindrical coordinates suitable for the analysis of traveling wave MRI applications," *Int. J. Numer. Model. Electron. Netw. Devices Fields*, vol. 26, no. 6, pp. 680–696, 2013, doi: 10.1002/jnm.1875.
[59] A. Fedeli, C. Montecucco, and G. L. Gragnani, "Open-source software for electromagnetic scattering simulation: The case of antenna design," *Electronics*, vol. 8, no. 12, p. 1506, Dec. 2019, doi: 10.3390/electronics8121506.
[60] G. Mur, "Absorbing boundary conditions for the finite-difference approximation of the time-domain electromagnetic-field equations," *IEEE Trans. Electromagn. Compat.*, vol. EMC-23, no. 4, pp. 377–382, Nov. 1981, doi: 10.1109/TEMC.1981.303970.

VALENTINA SCHENONE received the B.Sc. degree in electronic engineering and information technologies and the M.Sc. degree in electronic engineering from the University of Genoa, Italy, in 2018 and 2020, respectively, where she is currently pursuing the Ph.D. degree in science and technology for electronic and telecommunication engineering. Her research activity is focused on novel inversion techniques for electromagnetic imaging.

ALESSANDRO FEDELI (Member, IEEE) received the B.Sc. and M.Sc. degrees in electronic engineering and the Ph.D. degree in science and technology for electronic and telecommunications engineering from the University of Genoa, Genoa, Italy, in 2011, 2013, and 2017, respectively, where he is currently an Assistant Professor with the Department of Electrical, Electronic, Telecommunications Engineering, and Naval Architecture. He has coauthored more than 150 scientific contributions published in international journals, conference proceedings, and book chapters. His research activities are mainly focused on computational methods for the solution of forward and inverse scattering problems, and electromagnetic imaging.

CLAUDIO ESTATICO received the "Laurea" degree in mathematics from the University of Genoa, Genoa, Italy, in 1995, and the Ph.D. degree in computational mathematics and operation research from the University of Milan, Milan, Italy, in 2002. In 2003, he was a participant in the semester program on inverse problems with the Institute for Pure and Applied Mathematics, University of California at Los Angeles, Los Angeles, CA, USA. He is currently an Associate Professor of Numerical Analysis with the Department of Mathematics, University of Genova. He has authored or coauthored about 130 journal and conference papers. His research interests are numerical linear algebra and inverse problems. They include regularization in Banach spaces, preconditioning, iterative methods for linear and nonlinear ill-posed problems, with application in image restoration, industrial and biomedical microwave inverse scattering, and remote sensing.

MATTEO PASTORINO (Fellow, IEEE) is a Full Professor of Electromagnetic Fields with the University of Genoa, Genoa, Italy, where he is the Vice Rector for Technology Transfer. He was the Director of the Department of Electrical, Electronic, Telecommunications Engineering, and Naval Architecture, University of Genoa until 2021. He has coauthored about 500 articles in international journals and conference proceedings. His research interests include microwave and millimeter-wave imaging, direct and inverse scattering problems, industrial and medical applications, smart antennas, and analytical and numerical methods in electromagnetism. He is the Chair of the National URSI Commission B (Fields and Waves) and the Vice Director of the Interuniversity Center for the Interaction between Electromagnetic Fields and Biosystems. He is an Associate Editor of the *IEEE Antennas and Propagation Magazine* and the IEEE OPEN JOURNAL OF ANTENNAS AND PROPAGATION.

ANDREA RANDAZZO (Senior Member, IEEE) received the Laurea degree in telecommunication engineering and the Ph.D. degree in information and communication technologies from the University of Genoa, Italy, in 2001 and 2006, respectively, where he is currently a Full Professor of Electromagnetic Fields with the Department of Electrical, Electronic, Telecommunication Engineering, and Naval Architecture. He has coauthored the book *Microwave Imaging Methods and Applications* (Artech House, 2018) and about 300 articles published in journals and conference proceedings. His primary research interests are in the field of microwave imaging, inverse-scattering techniques, radar processing, numerical methods for electromagnetic scattering and propagation, electrical tomography, and smart antennas.